Shuttle Imaging Radar Experiment

Abstract. *The shuttle imaging radar (SIR-A) acquired images of a variety of the earth's geologic areas covering about 10 million square kilometers. Structural and geomorphic features such as faults, folds, outcrops, and dunes are clearly visible in both tropical and arid regions. The combination of SIR-A and Seasat images provides additional information about the surface physical properties: topography and roughness. Ocean features were also observed, including large internal waves in the Andaman Sea.*

On its second flight in November 1981, the space shuttle Columbia carried its first scientific payload into earth orbit. Part of this payload was the shuttle imaging radar (SIR-A), which acquired radar images of about 10 million square kilometers around the world. These images of a variety of geologic regions in different physiographic settings should enhance our understanding of the uses of radar imagery, alone as well as in conjunction with other remote sensing data, for geologic mapping. In this report the SIR-A experiment and some of the preliminary scientific results are described, including the sensor and the performance it achieved during the mission and examples of the data analyzed from a number of geoscience disciplines—structural geology, geomorphology, cartography, land use, and oceanography.

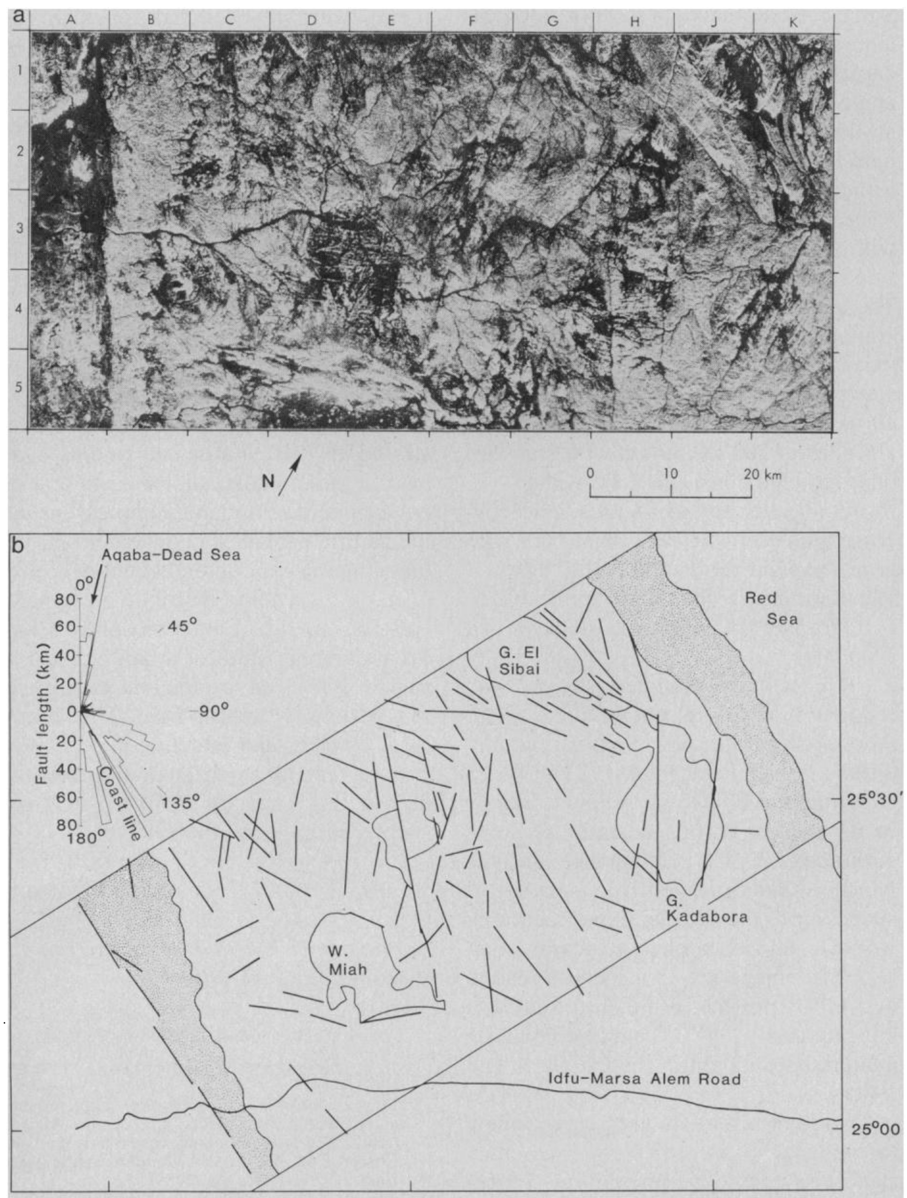

Fig. 1. (a) SIR-A image of an area in the southeastern desert of Egypt, (b) Lineament map with a rose diagram (insert, upper left) of lineaments longer than 5 km.

The SIR-A sensor is a synthetic aperture imaging radar which produces high-resolution images of the surface by the use of the time delay and Doppler history of the returned echoes (*1*). The radar sensor generates a high peak power signal which is frequency-modulated and is radiated through a planar array antenna toward the earth's surface. Part of the returned echo is collected by the antenna, amplified and detected by the receiver, and coherently recorded on optical film. This "signal" film contains a record of the returned echoes in holographic form. The film retrieved from the shuttle was processed in an optical correlator, where the synthetic aperture is effectively formed. From the information from thousands of echoes, the high-resolution image is generated and recorded on the image film. The image is a two-dimensional representation of the surface scattering which in turn is a function of the surface physical properties—that is, slope, roughness, and dielectric constant (*2*). The SIR-A sensor was designed to acquire surface images with a resolution of 40 meters. Other SIR-A characteristics are summarized in Table 1. The sensor was in operation for 8 hours during the 2½-day flight. Images were acquired over regions with surface covers that ranged from tropical forests in the Amazon and Indonesia to the completely arid deserts of North Africa and Saudi Arabia.

During the flight, two engineering experiments were conducted to determine the sensor performance. Corner reflectors were deployed near Lake Henshaw in southern California to provide a number of bright targets, smaller than the resolution elements, for measuring the point response of the sensor, particularly its resolution and sensitivity. A good image of the corner reflector array verified that a resolution of 40 m was obtained. In the second experiment, ground receivers measured the energy incident on the surface as the shuttle passed by. This would allow characterization of the antenna pattern and the determination of changes caused by interference from the shuttle structure. The pattern obtained during the flight and during a laboratory test were almost indistinguishable.

Land observation. Imaging radar data have been particularly useful in geologic structural mapping because radar scattering is sensitive to surface topography over a wide range of scales. Surface structural features such as lineaments,

0036-8075/82/1203-0996$01.00/0

faults, fractures, domes, layered rocks, and outcrops often cause recognizable variations in surface topography, cover, or roughness. Examples of some of the structures observed with the SIR-A are described below.

1) Lineament mapping:

The SIR-A image and corresponding interpretation of an area in the southeastern desert of Egypt (Fig. 1) focus on a region of late Precambrian shield which, for the most part, has been tectonically stable for the last 500 million years. Accumulation of sand in wadis produces a dark tone on the radar image because of the smooth surface. Narrow wadis often mark the location of major faults, where selective erosion has occurred. The Cretaceous Nubian Sandstone onlaps the Precambrian shield on its western boundary. These outcrops have a relatively bright albedo because of the rough, eroded surface and are also characterized by well-developed dendritic drainage. Granitic plutons are generally circular in shape and have a dark center, corresponding to relatively smooth areas that have eroded rapidly relative to the country rock. In some cases, the granitic plutons have dike swarms or parallel joint fractures, and these are readily distinguished on the image. Many of the granite plutons were intruded in a geologically narrow time span, about 575 million to 600 million years (*3*). In some cases, an older syntectonic suite of granodioritic plutons can be recognized because of the strong erosion and consequent dark appearance. The plutons provide an important age constraint on the lineament analysis.

Many of the lineaments that are longer than 5 km (Fig. 1b) most likely represent faults because of observed feature offset. Three sets of lineaments are apparent. The set striking nearly west does not cut any of the granite plutons and thus is probably the oldest. A second lineament set trends at about N45°W, which is approximately parallel to the coast of the Red Sea. Since this group displaces outcrops of the Cretaceous Nubian Sandstone, or at least strongly controls its

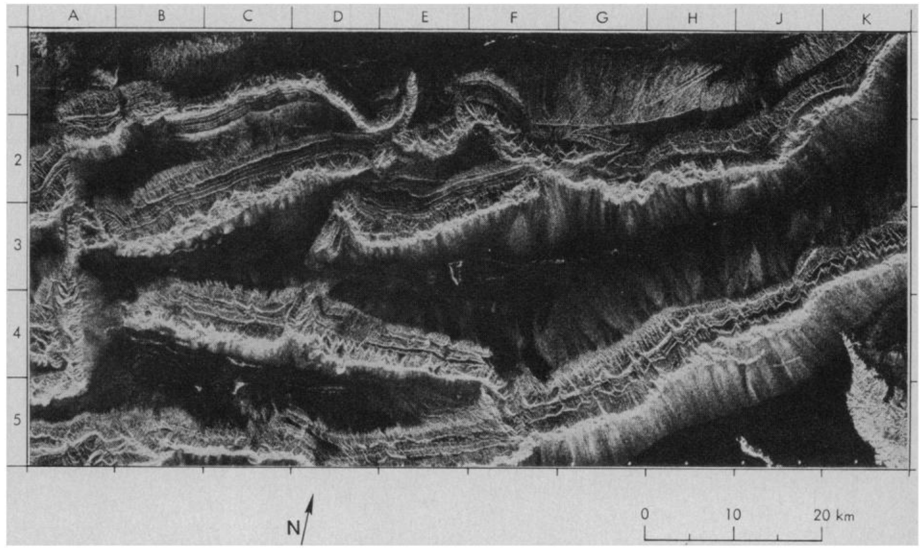

Fig. 2. SIR-A image of part of the Kelpin Tagh uplift region in northwestern China.

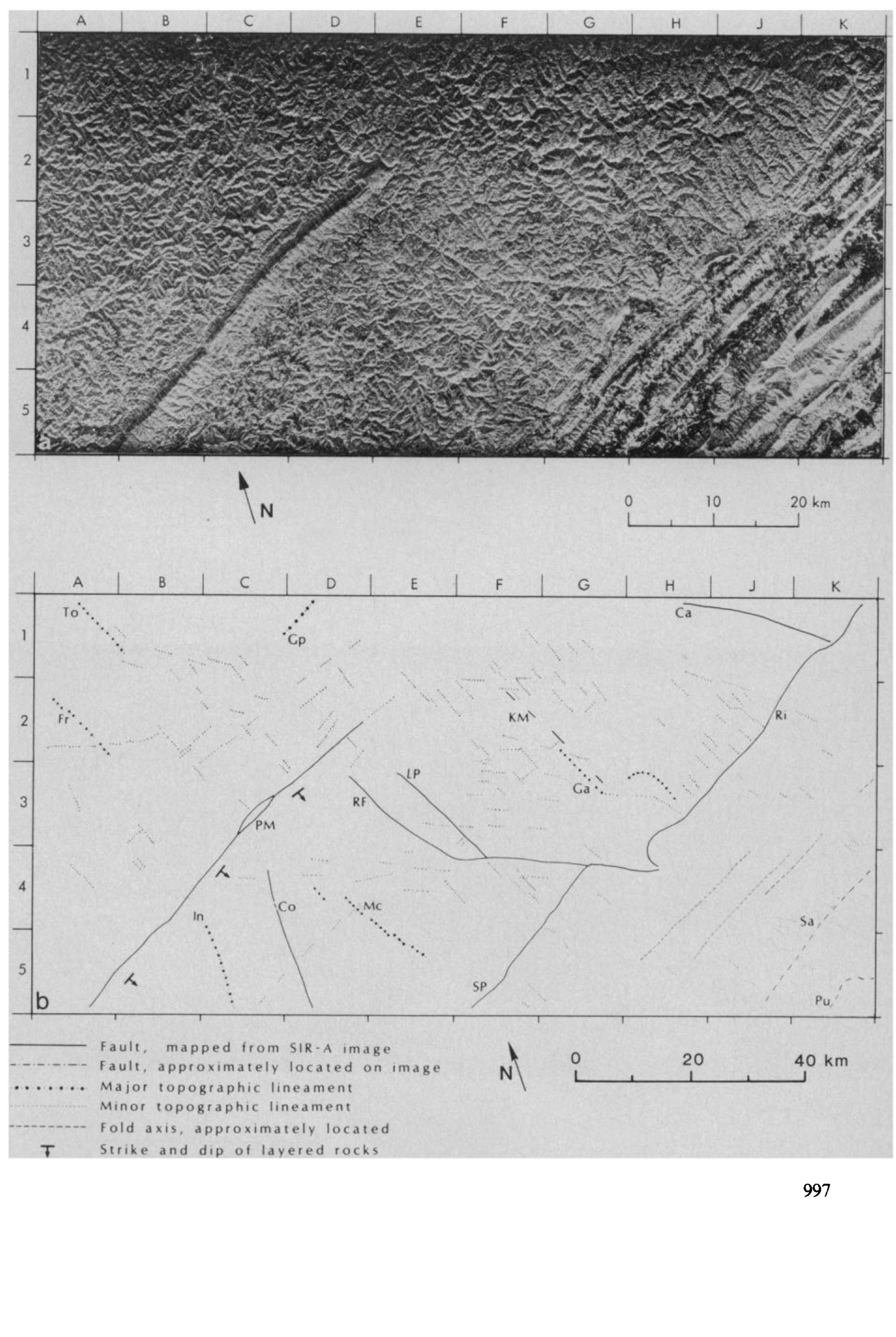

Fig. 3. (a) SIR-A image of part of the Appalachian Plateau in southeast Kentucky. (b) Lineament map derived from SIR-A image showing major faults and fold areas. Labeled faults are *PM*, Pine Mountain; *Co*, Coeburn; *RF*, Russell Fork; *Ca*, Canebrake; *LP*, Little Paw Paw Creek; *KM*, Keen Mountain; *SP*, St. Paul; *Ri*, Richlands; *Sa*, Saltville; and *Pu*, Pulaski. Labeled major lineaments are *To*, Toler Creek; *In*, Indian Creek; *Fr*, Frasure Creek; *Gp*, Grapevine Creek; *Ga*, Garden Creek; and *Mc*, McClure Creek.

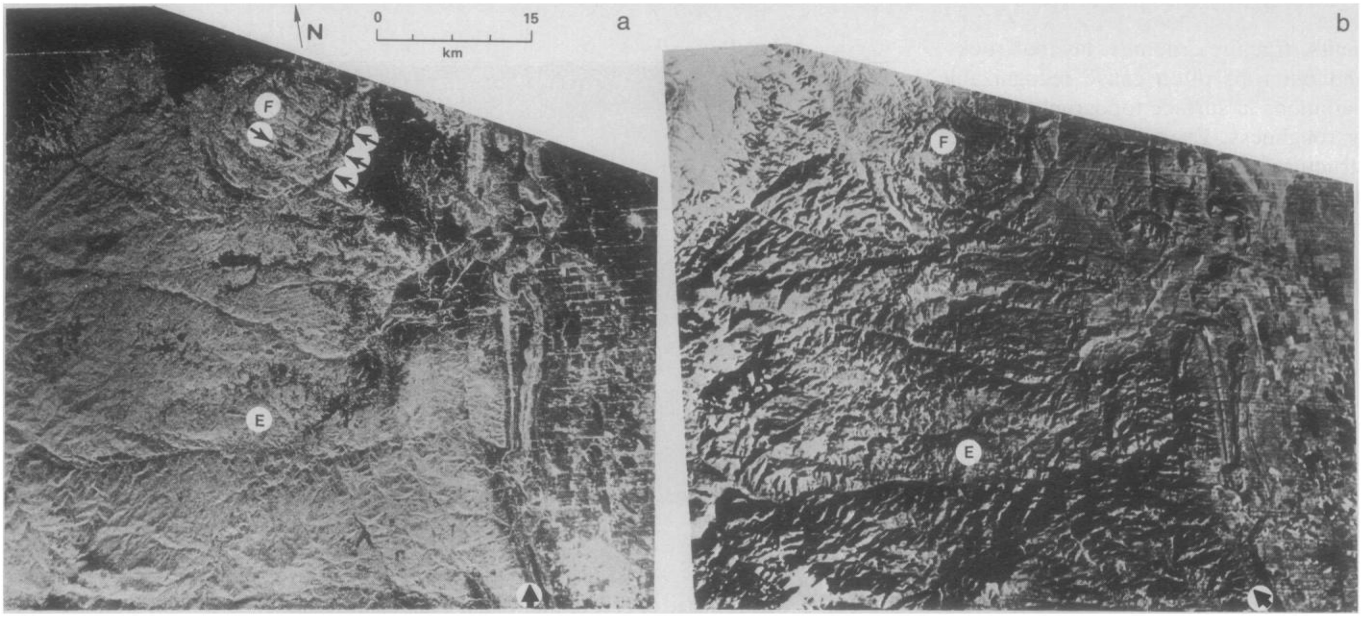

Fig. 4. (a) SIR-A and (b) Landsat images of the Virginia Dale ring-dike complex. The Landsat image was acquired December 1976. The solar elevation was 20° above the horizon with an azimuth angle of 149°. The SIR-A look direction was about N10°E.

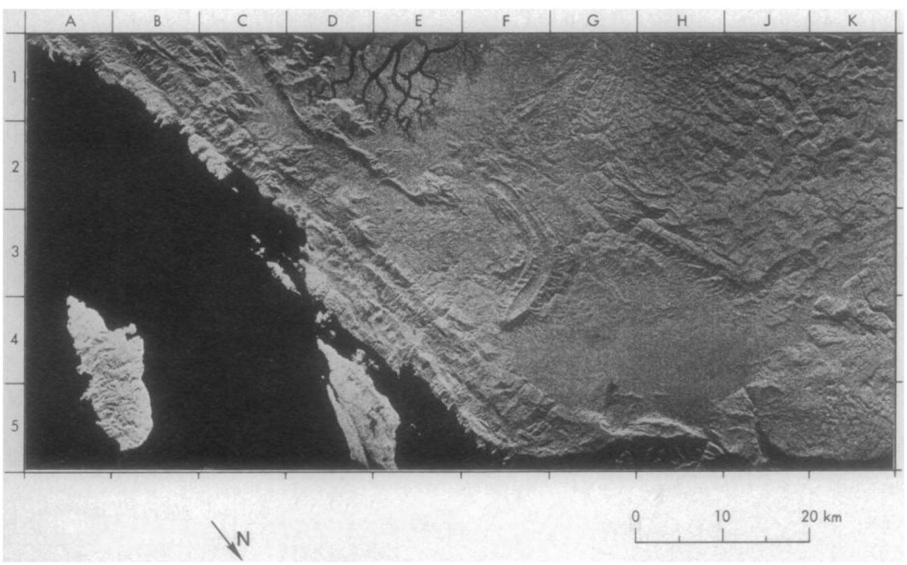

Fig. 5. Part of the Lengguru Fold Belt in New Guinea.

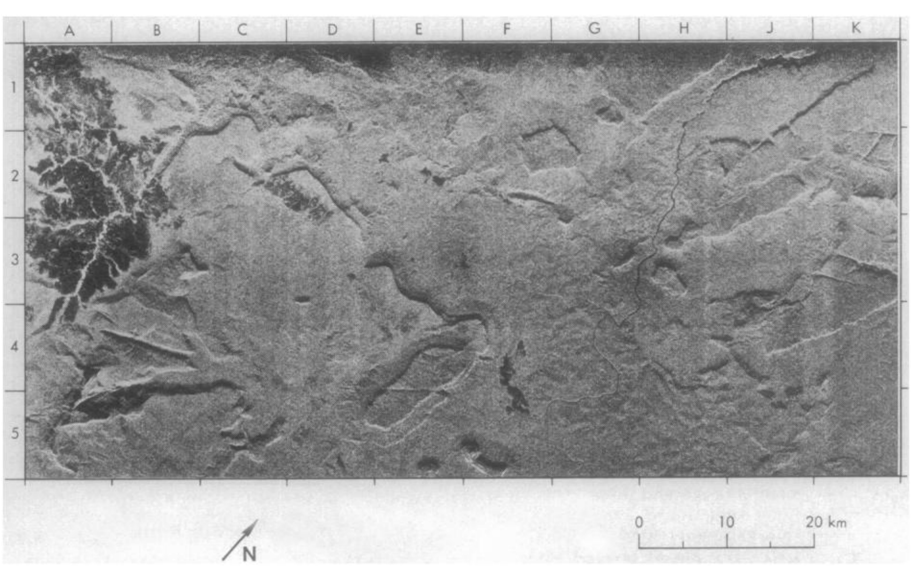

Fig. 6. SIR-A image over the Pakaraima Mountains near the boundary between Guyana and Venezuela.

deposition, it must have been active in Mesozoic time. The strongest linear feature on the image is the northwest-trending boundary in the Nubian Sandstone, which separates two areas of appreciably different surface characteristics. This boundary seems to be an extension of mapped faults to the north and south and therefore would be part of one of the longest well-defined lineaments in the eastern desert, with a strike length of at least 250 km.

A third set of lineaments (trending N10°W to N5°E) is approximately parallel to the direction of the Dead Sea–Gulf of Aqaba Fault, an active left-lateral transform fault associated with Tertiary to Recent opening of the Red Sea. Many lineaments in this group are observed to cut the posttectonic granitic plutons in the radar image. One obvious fault in this group displaces an older lineament and a granitic pluton by about 2 km in a left-lateral sense. It is also approximately on strike with the Aqaba Fault. This alignment and left-lateral motion, coupled with the age constraints on this lineament set (derived from observed displacement of granitic plutons), suggests that these faults are Mesozoic or younger and are associated with the Red Sea rift-transform system. It is also possible that this set of faults is Precambrian in age but was reactivated during the opening of the Red Sea. In this case, preexisting tectonic trends in the shield would have controlled the orientation of the Red Sea rift.

Images of the Kelpin Tagh uplift in northwestern China (Fig. 2) illustrate large-scale faulting. Faults are visible because of the displacement of the sedimentary rocks that control the topography. The stratified sandstones, limestones, and shales exposed on the upper portions of the cuestas (hogbacks) are easily delineated on the image. The alluvial fans that are pervasive below the cuestas are also well defined on the radar image because of the sensitivity of the *L*-band radar (23-cm wavelength) to small changes in gravel sizes and the strong increase in Rayleigh scattering at about the 4 to 6 cm mean relief scale, as described (*4*) in Death Valley, California. The playas are characterized by dark tones because of their smooth surfaces.

The SIR-A image of the Appalachian Plateau in southeast Kentucky (Fig. 3a) shows an area that is fully covered by a dense forest of mixed deciduous and coniferous trees and is deeply dissected. A major structural feature is the Pine Mountain overthrust, where a plate of plateau rocks has been carried northeast for a distance of about 6.4 km over ridge

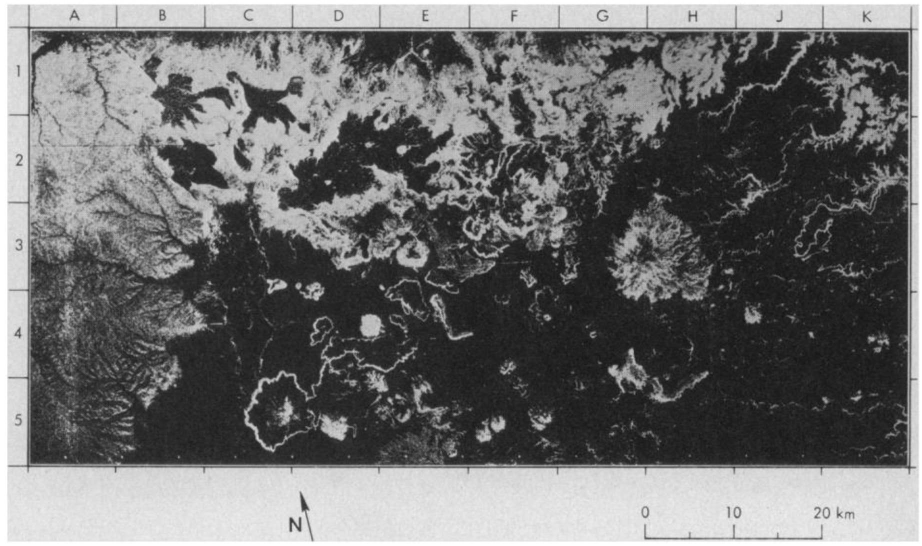

Fig. 7. SIR-A image of a volcanic field west of Raton, New Mexico.

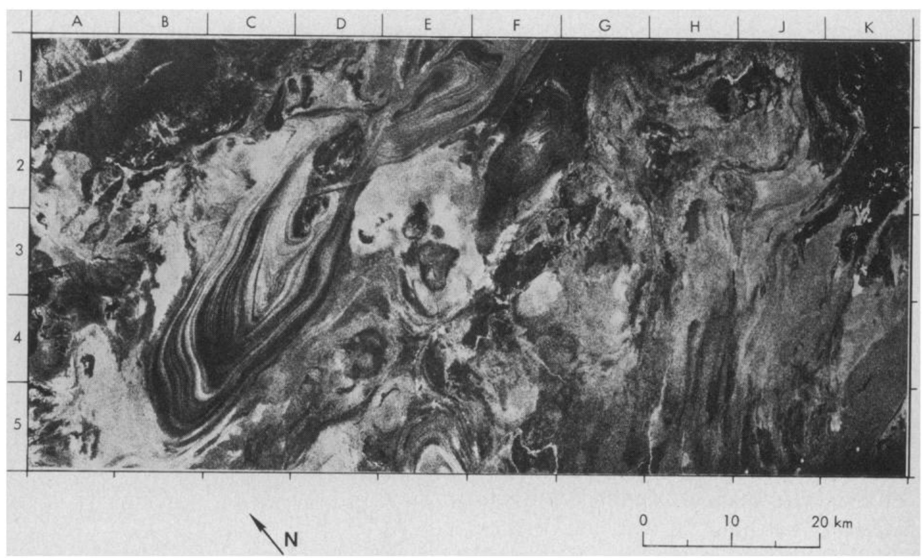

Fig. 8. SIR-A image of the northern part of the great Kavir Salt Desert in Iran.

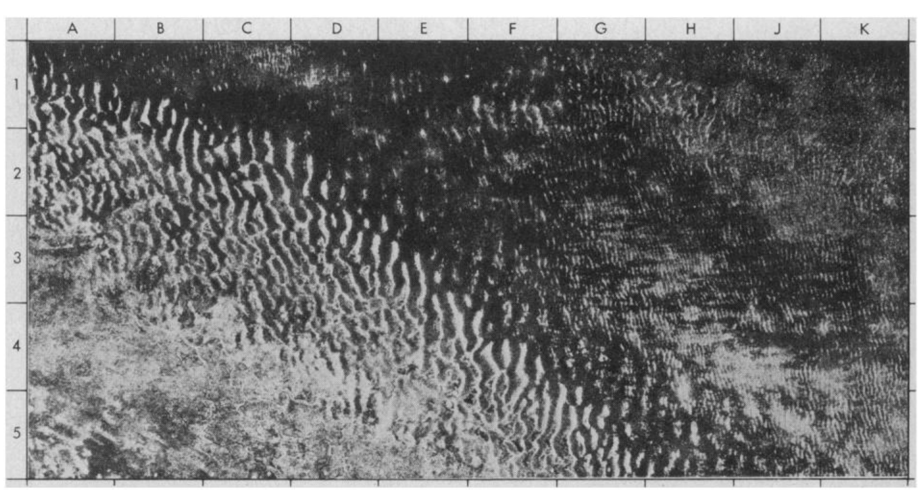

Fig. 9. SIR-A image of a regional sand sea in the Lake Chad Basin northwest of N'Djamena, Chad.

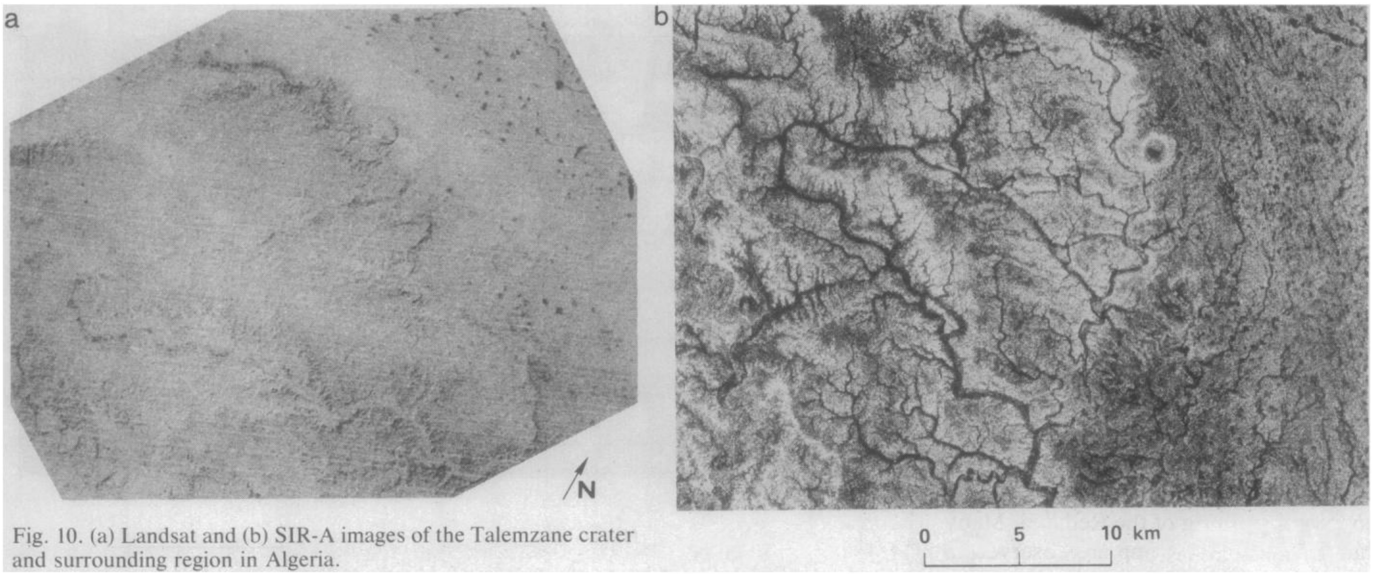

Fig. 10. (a) Landsat and (b) SIR-A images of the Talemzane crater and surrounding region in Algeria.

and valley rocks (5). On the lineament map derived from the SIR-A image (Fig. 3b) linear valleys or alignments of valley segments that are 15 km or longer correspond primarily with mapped faults from published sources. Shorter lineaments are primarily oriented parallel to fault trends. This parallelism suggests that the lineaments are most likely structural in origin, a suggestion supported by the observation that the Toler Creek, Grapevine Creek, and Frasure Creek lineaments are oriented approximately parallel to structure contours on the subsurface Ohio Shale (6). The shorter lineaments also trend nearly parallel with linear segments of a strong magnetic gradient in the basement shown on the aeromagnetic map of Kentucky. Also, fieldwork has shown that the Indian Creek lineament is the site of faulted rocks.

The detection of linear fractures with a radar or a visible wavelength sensor is strongly dependent on the illumination geometry. This is illustrated by the Landsat and SIR-A images (Fig. 4) of the Virginia Dale ring-dike complex along the Colorado–Wyoming Front Range. The fracture patterns in the igneous complex, which trend north-northwest (feature F), are clearly visible on the SIR-A image, where the illumination is almost perpendicular to the direction of the fractures. The pattern is barely visible on the Landsat image because the solar illumination is oriented almost parallel to the fracture trend. The opposite situation occurs in the case of the linear feature that is visible on Landsat but not on SIR-A (feature E). Thus, in order to get a more comprehensive lineament map, both Landsat and SIR-A data are needed.

2) Fold structures:

Fold structures are recognized because of their shape and form as observed on visible or radar images. The folding of the rocks and the subsequent erosion lead to characteristic patterns of topography, surface roughness, or vegetation cover. Figure 5 shows a folded structure in the Lengguru belt in New Guinea. This is a densely forested area

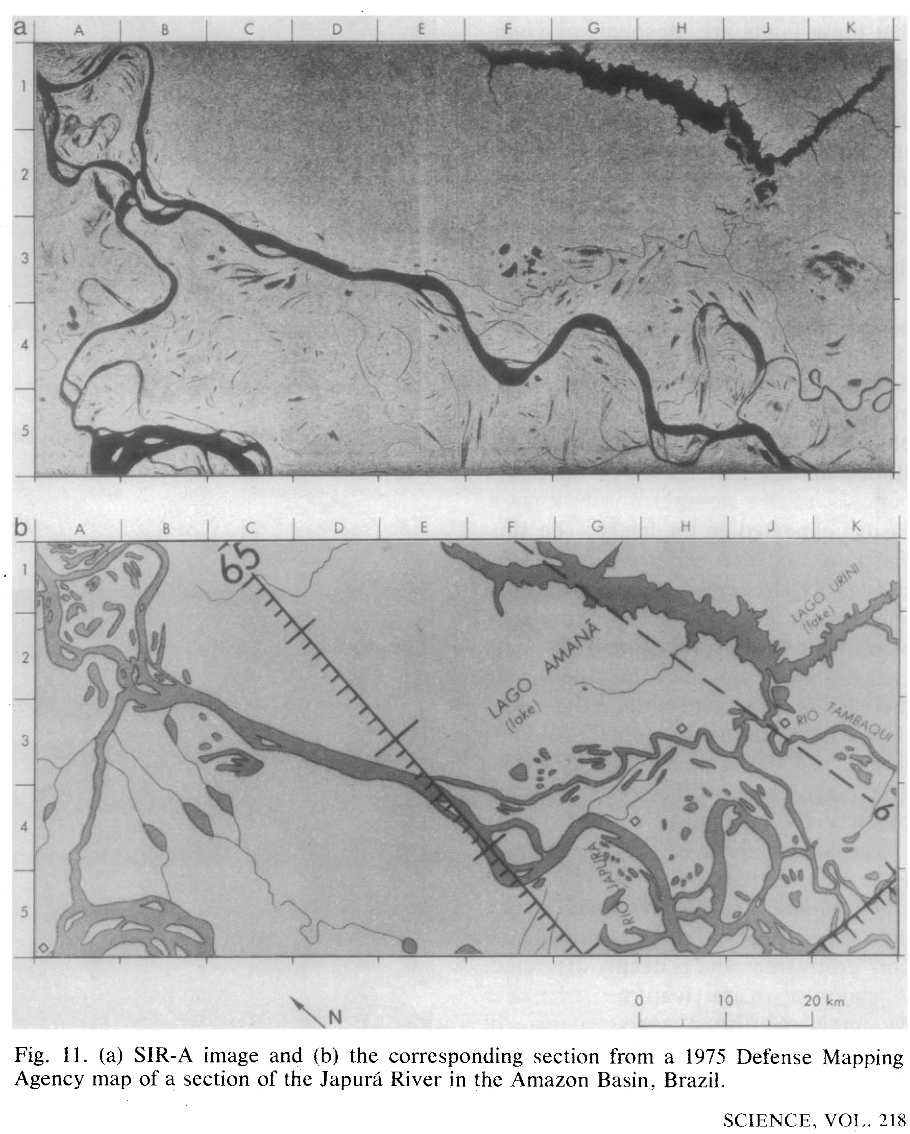

Fig. 11. (a) SIR-A image and (b) the corresponding section from a 1975 Defense Mapping Agency map of a section of the Japurá River in the Amazon Basin, Brazil.

where the folded structure is observed because of variations in the topography.

3) Dissected plateaus:

The SIR-A image of the Pakaraima mountains in western Guyana (Fig. 6) shows an area of dissected plateaus and mesas with an elevation of about 1000 to 1500 m. Considerable structural details can be seen despite the complete rain-forest cover. Foliation trends, fractures, and major lithological units can be distinguished although fieldwork is necessary to ascertain lithological detail. Deep precipitous canyons have been eroded into the plateau. The canyons are enhanced on the image from the bright returns at the foreslopes and from shadowing at the backslopes. The upland is directly underlain by flat-lying sedimentary rocks of the Proterozoic Roraima Formation. Extensive linear stream valleys and drainages in the plateau area are structurally controlled. Linear offsets of the channels follow joints and faults. The wide lowland valleys are underlain mostly by basic igneous intrusive rocks of Mesozoic age, and stream channels meander in the lowland valleys. There is a subtle textural difference on the radar image between the plateau and the lowland valleys. This area of Guyana and the adjacent Gran Sabana of Venezuela are exceptionally inaccessible.

4) Volcanic fields:

Volcanic lava flows are usually characterized by bright radar albedo because of their surface roughness, and recent flows may be associated with recognizable volcanic features. On the SIR-A image of a volcanic field west of Raton, New Mexico, the brightest feature is Sierra Grande (Fig. 7, H-3), a large intrusive mass of dacitic volcanic rocks. These rocks are of higher silica and alumina content than the common basaltic lava flows. They form coarse-grained talus that slides down the slope. These coarse fragments give a bright radar return. In contrast, Eagle Tail Mountain (C-5) is a volcanic center surrounded by lava flows of basaltic composition. The main body of the flow gives a low return. The margins of these flows chilled during eruption and were broken up by the continued flow. Most of the blocks slid down the edge of the flow forming a blocky talus. Thus the flow is outlined by a bright band as seen in the image.

5) Salt pans:

The SIR-A image of the northern part of the Great Kavir region in Iran (Fig. 8) shows this extensive salt desert that consists of a subtle combination of salt-encrusted playa basins surrounded by folded and eroded Miocene rocks, which are mostly evaporites. The evaporites

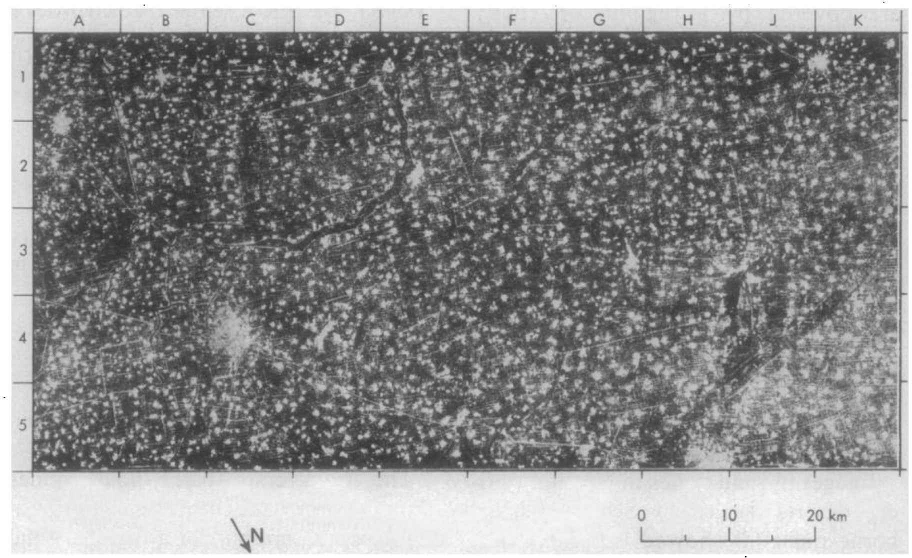

Fig. 12. SIR-A image illustrating cultivated fields and towns north of Chinan, China.

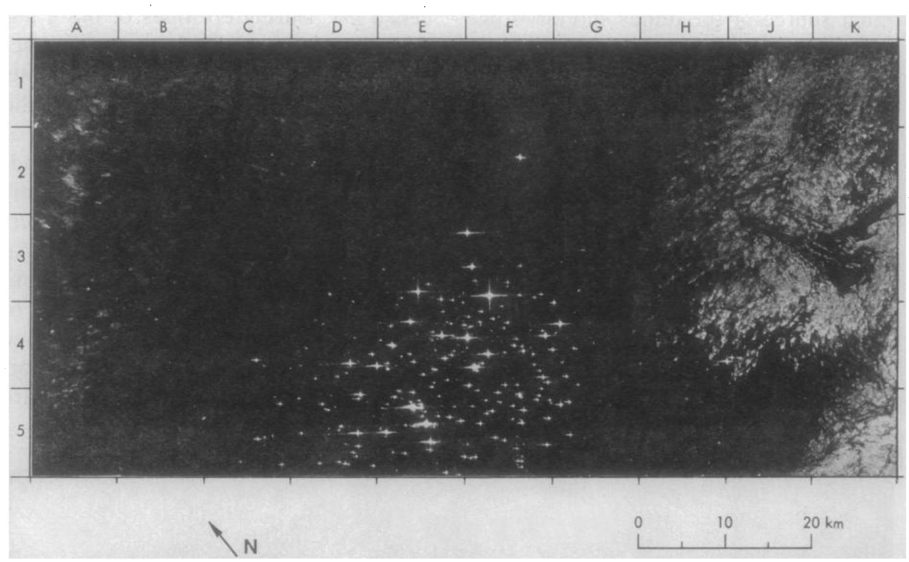

Fig. 13. SIR-A images of part of the Arabian Sea showing numerous oil platforms and ocean vessels.

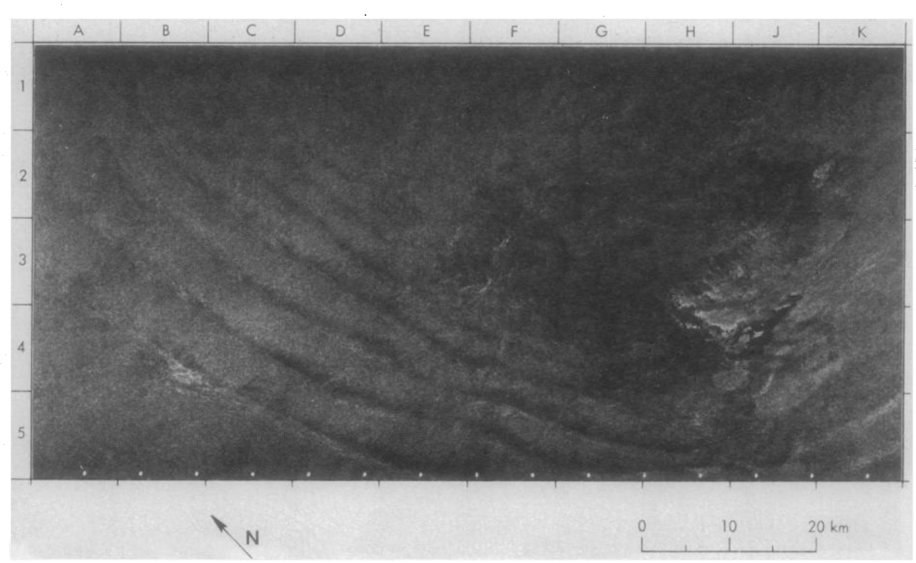

Fig. 14. SIR-A image of a large internal wave train in the Andaman Sea. The data were acquired on 14 November at 10:56 GMT.

are covered by a regolith of "puffy ground," up to a meter thick, caused by alternate wetting and drying of the weathered bedrock and consequent churning of the silts and clays that make up the surface (*7*). Locally the surface is punctured by spectacular salt diapirs. The salt flats have a wide range of bright variations on the radar image, corresponding to the variation in the surface roughness. In some areas strata of the folded Miocene bedrock can be seen clearly on the radar image though they are difficult to discern on the ground because of the in situ regolith.

6) Sand dunes and sand streaks:

Images of sand dunes in North American deserts imaged by Seasat and airborne radar (*8*) showed that these features give a dark response typical of smooth surfaces unless dune facets are oriented approximately normal to the radar source or the dunes support some vegetation. The illumination direction is also critical in attaining images of dune patterns, which identify the morphological type. Such morphologic identification is essential if dunes are to be used to interpret causative wind regimes.

These observations agree with those of SIR-A images of large dune fields in Africa and Asia. Images were acquired over parts of several major deserts including the Taklamakan, Badain Jaran, Ulan Buh, and Mu Us deserts in China; the Kara Kum desert in the Soviet Union; the An Nafud in Saudi Arabia; and the Sahara of northern Africa.

Table 1. The SIR-A sensor characteristics.

Parameter	Value
Frequency	1.3 Ghz
Wavelength	23 cm
Polarization	HH
Look angle	47° ± 3°
Incidence angle at surface	50° ± 3°
Image swath width	50 km
Image resolution	40 × 40 m
Antenna size	2.1 × 9.5 m
Area covered	10^7 km^2
Average orbital altitude (km)	259 km

The transverse (barchanoid) dunes (Fig. 9) in the Lake Chad Basin of N'Djamena, Chad, are part of a regional sand sea built by Saharan winds from reworked alluvium during one or more episodes of aridity, when the lake receded (*9*). During episodes of more humid climatic conditions, the lake rose, flooded the dunes, and left diatomaceous deposits capped by limy beds in the interdune hollows. Regional recession of the lake has left large dune ridges standing above interdune flats that are characterized by abandoned or ephemeral drainage channels, wind-eroded lake beds, rough salt playas, and vegetation. These surfaces give a wide variety of signatures on the SIR-A image. The dune ridges, whose long axes are aligned parallel to the direction of illumination, are mostly dark. The bright patterns correspond to the strong return from the heavily vegetated interdune flats. The irregular outlines of the sand ridges are typical of vegetated, inactive dunes that have been weathered and eroded under conditions of climatic oscillations.

7) Craters:

Recent impact craters, such as the Talemzane crater in eastern Algeria (Fig. 10, a and b) are characterized by rough ejecta rims that may be recognizable on radar images. The Talemzane crater is 1.75 km in diameter and 70 m deep. It was dated at about 0.5 to 2 million years old (*10*). The bright halo on the SIR-A image (Fig. 10b) corresponds to the rough ejecta on the rim. Field observations (*10*) indicated that blocks up to a size of 1m are not uncommon. Figure 10 also illustrates the superior capability of SIR-A (Fig. 10b) radar sensors, relative to visible sensors (Fig. 10a), in portraying some of the surface features in arid regions. The dendritic dry drainage channels are highlighted on the radar image most likely because of the sand filling of their stream channels. In the visible part of the spectrum the albedo of the filling sand seems to be close to the albedo of the surrounding country rock, leading to the subdued expression of the surface features.

8) Cartography in remote regions:

Radar sensors are insensitive to cloud cover, a feature that is particularly help-

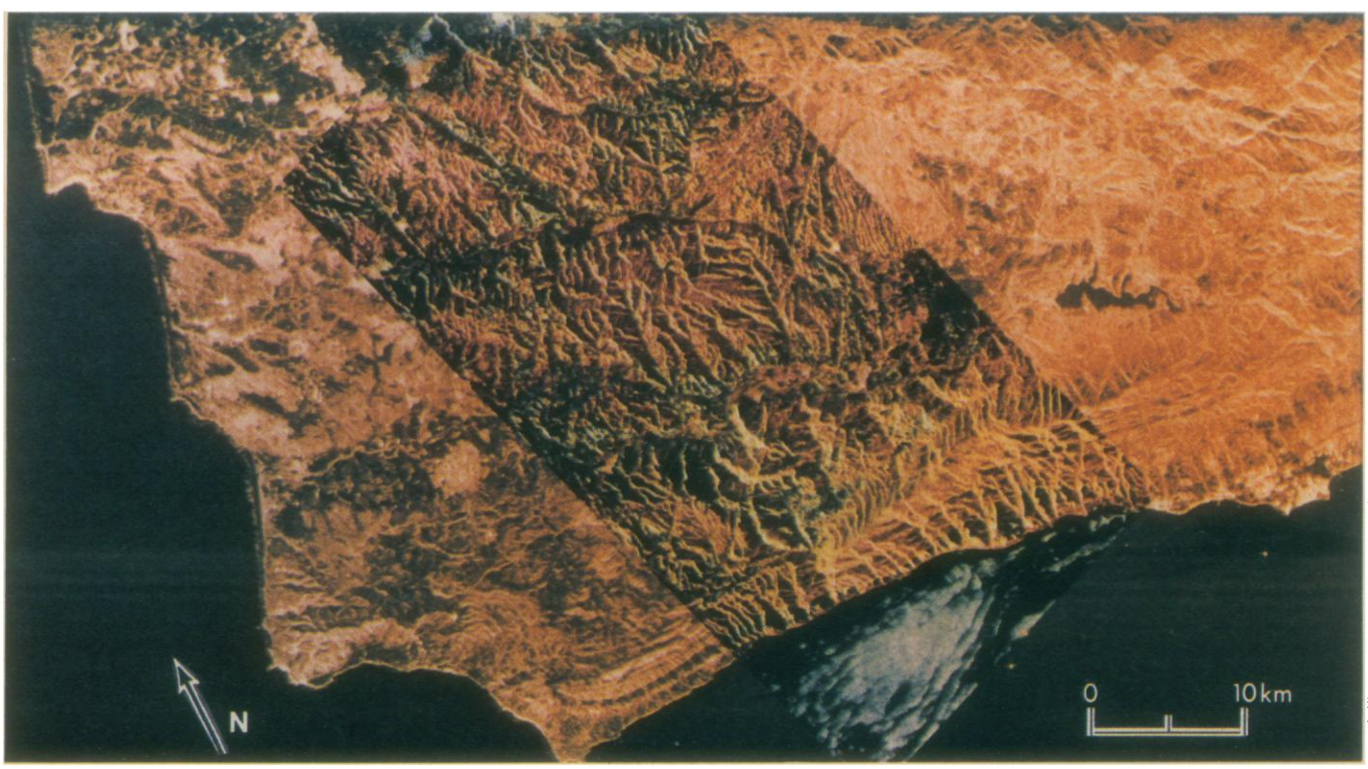

Fig. 15. Color composite image of digitally coregistered SIR-A and Seasat images of the southern California coastal area near Santa Barbara. The SIR-A data correspond to the color and the Seasat data (rectangular insert) to the intensity.

ful in mapping tropical regions where cloud cover is extensive and surface access is difficult. Such a region is the Amazon, where most recent maps of the major surface features are still not accurate. Comparison of the SIR-A image to the most recent (1975) Defense Mapping Agency map shows major discrepancies at the junction of the Amazon and Jupurá rivers, which are most likely a result of errors in the mapping (Fig. 11, a and b).

9) Land use:

The radar scattering is strongly controlled by small-scale roughness, surface vegetation, and man-made structures. Urban regions strongly backscatter the radar signal either because the walls of buildings form corner reflectors with the surface, or because of the abundance of metallic structures, or both. Towns, villages, and roadways are delineated in the SIR-A image of the region north of Chinan in northeastern China (Fig. 12). Because of their strong return, man-made structures can usually be observed even if their physical size is smaller than the sensor resolution, as shown in Fig. 13, which shows the radar images of oil platforms in the Arabian Sea.

Ocean surface features. The SIR-A sensor was configured for land observation. The resolution of 40 m precluded imaging small- to medium-size ocean swells, and the large incidence angle resulted in a relatively low return from the ocean surface. In a number of cases, however, large ocean features were observed, such as an internal wave train in the Andaman Sea (Fig. 14). Numerous large internal waves have been observed in that region and confirmed by surface observations (*11*). The mechanisms which allow the radar imaging of such ocean features have been discussed by Elachi and Apel (*12*) and Elachi (*13*) in the case of airborne radar sensors and the Seasat SAR. The same mechanisms are most likely at work in the case of SIR-A.

Use with other sensors. Remote sensors provide different information about the surface as a function of the spectral and polarization characteristics of the sensor and the observation geometry. Visible and near-infrared sensors provide information mostly about the composition of the surface material. Thermal infrared sensors provide information about the surface and bulk thermal properties of the near surface layer. Radar sensors provide information mainly about the surface physical properties. In order to acquire a detailed description of the surface, information from more than one sensor is required. Analysis of coregistered Landsat and Seasat images of the San Rafael region in Utah indicated that the addition of radar data enhances the capability to separate lithologic units (*14*).

Even when the same type of sensor is used, changes in the illumination geometry can be important. Particularly in the case of the radar sensor, observation at a near vertical incidence angle (around 20° to 30°) enhances the surface slope, and observation at an intermediate angle (40° to 60°) enhances surface roughness (*2*, *4*). This effect is clearly illustrated by analyzing Seasat and SIR-A images of the same areas. Both sensors are identical except for the changes in the incidence angle (20° for Seasat and 50° for SIR-A) and in the look direction. Figure 15 shows a registered Seasat–SIR-A image of part of the Santa Ynez mountains in southern California. The SIR-A data were used to produce the color, and the Seasat data were used to modulate the intensity of the color where the images overlap. The combination of surface roughness and topographic information shown in this image allows better discrimination of the lithologic units present. The topographic information provided by the Seasat data enhances the image texture, which can be used to differentiate rock types. For example, the linear and fine-scale texture pattern at the upper right-hand edge of the Seasat image (the rectangular insert) is related to nonmarine unconsolidated conglomerates. In the center of the image is a coarse mountainous texture related to marine sandstones. The SIR-A image, on the other hand, shows bedding patterns along the coast that cannot be seen in the Seasat image alone.

The SIR-A experiment extends the capability achieved with the Seasat imaging radar in observing surface features and complements the capability of visible and infrared imaging sensors. Because of its sensitivity to the surface physical properties, the SIR-A sensor provides information about surface structure, cover, and roughness that can be used in geologic or oceanographic investigations. It also provides a basis for the analysis of data that will be acquired with planetary orbiting radars planned for imaging the surfaces of Venus and Titan.

The SIR-A experiment, in conjunction with the others on the second shuttle flight, demonstrates the useful role of the space shuttle as a platform for scientific investigations. The SIR-A sensor was returned from space in fully operational status and is being modified and upgraded for reflight in 1984. This upgraded sensor, SIR-B, will allow experimentation with variable illumination geometries, stereo imaging, higher spatial resolution, and digital data-handling capability.

C. ELACHI
W. E. BROWN, J. B. CIMINO
T. DIXON, D. L. EVANS
J. P. FORD, R. S. SAUNDERS
Jet Propulsion Laboratory, California Institute of Technology, Pasadena 91109
C. BREED
H. MASURSKY
J. F. MCCAULEY
G. SCHABER
U.S. Geological Survey, Flagstaff, Arizona 86001
L. DELLWIG
University of Kansas, Lawrence 66044
A. ENGLAND
Johnson Space Flight Center, Houston, Texas 77058
H. MACDONALD
University of Arkansas, Fayetteville 72701
P. MARTIN-KAYE
Huntington Geology and Geophysics, London, England WD6 15B
F. SABINS
Chevron Oil Field Research, La Habra, California 90631

References and Notes

1. C. Elachi, *Science* **209**, 1073 (1980); see also H. Jensen, L. J. Porcello, E. N. Leith, *Sci. Am.* **237**, 84 (October 1977).
2. F. F. Sabins, *Remote Sensing, Principles and Interpretation* (Freeman, San Francisco, 1978).
3. P. D. Fullagor and J. K. Greenberg, *Precambrian Res.* **6**, A-22 (1978).
4. G. G. Schaber, L. Berlin, W. E. Brown, Jr., *Bull. Geol. Soc. Am.* **82**, 29 (1975).
5. L. D. Harris and R. C. Milici, *U.S. Geol. Surv. Prof. Pap. 1018* (1977).
6. L. P. Fulton, Kentucky Geological Survey structure and isopach map of the New Albany–Chattanooga–Ohio Shale in Kentucky, eastern sheet series 11 (Lexington, Ky., 1979).
7. D. B. Krinsby, *Air Force Geophys. Lab. Rep. Air Force Cold Res. Lab. 70-0503* (1970).
8. R. Blom and C. Elachi, *J. Geophys. Res.* **86**, 3061 (1981).
9. A. T. Grove and A. Warren, *Geol. J.* **134**, 200 (1968).
10. P. Lambert, J. Mehone, R. Dietz, M. Houfani, *Meteoritics* **15**, 157 (1980).
11. A. R. Osborne and T. L. Burch, *Science* **208**, 451 (1980).
12. C. Elachi and J. Apel, *Geophys. Res. Lett.* **3**, 647 (1976).
13. C. Elachi, *Boundary-Layer Meteorol.* **13**, 165 (1978).
14. R. Blom and M. Daily, *IEEE Trans. Geosci. Remote Sens.*, in press.
15. As in every major experiment involving complicated sensors, success results from a team effort involving numerous people. We would like to acknowledge our colleagues at JPL and JSC who designed, developed, tested, and operated the SIR-A sensor. In particular we acknowledge the effort of G. Sisk (task manager), J. Granger (cognizant engineer), T. Andersen, E. Caro, H. Harris, S. Wall, and numerous other people at JPL who were part of the SIR-A implementation and operation team and of numerous people at JSC, particularly R. Moke, G. Kenny, H. Nitschke, and R. Baldwin, and at NASA, particularly K. Carver, B. Schardt, J. Taranik, and J. Welch. Supported by NASA's Office of Space Science and Applications.

20 August 1982